Journal of Building Engineering 111 (2025) 113604

Contents lists available at ScienceDirect

Journal of Building Engineering

journal homepage: www.elsevier.com/locate/jobe

The influence of restraint on salt frost damage of concrete: Deterioration of pores

Zhihao Gao [a,b,c], Zhendi Wang [c,*], Ling Wang [c], Yading Xu [d], Xia Zhao [c]

[a] Beijing Jiaotong University, School of Civil Engineering, Beijing, 100044, China
[b] China Communications Construction Company Highway Bridges National Engineering Research Centre Co., Ltd., Beijing, 100011, China
[c] China Building Materials Academy, Beijing, 100024, China
[d] Microlab, Delft University of Technology, the Netherlands

ARTICLE INFO

Keywords:
Restrained concrete
Single-side salt freezing and thawing
Strain
Relative humidity
Pore deterioration

ABSTRACT

Conventionally, during single-side freezing and thawing (SSFT) tests, concrete is permitted to deform freely. However, in practical scenarios, concrete is frequently surrounded by other materials or structures, which typically restricts its deformation when subjected to SSFT cycles. To simulate such service conditions during SSFT tests, a restraint ring and anchors are designed to confine the deformation of concrete. This study investigates the impact of restraint on the pore deterioration within concrete with a water - cement ratio of 0.60 under SSFT cycles. The internal relative humidity (IRH) and strain of both restrained and unrestrained concrete were monitored throughout the SSFT cycles. A comparison was made between the increment of IRH and residual strain of the restrained and unrestrained concrete. The results indicated that the increment of IRH and residual strain of the restrained concrete were 30 % lower than those of the unrestrained concrete. A simplified pore structure model was developed to calculate the strain resulting from pore deterioration. The rate of ice-crystal formation in restrained concrete was slower than that in unrestrained concrete. Additionally, the deformation strain and peak strain of pore deterioration caused by water freezing in concrete were respectively 55 % and 18 % lower than those in unrestrained concrete. Therefore, applying restraint effectively mitigates the internal damage of concrete subjected to SSFT cycles.

1. Introduction

Deicing salt is commonly used to melt snow on concrete structures, such as roads and bridges [1]. It has been found that deicing salt and snow-melt water often cause severe surface scaling and internal damage to concrete after cyclic freezing and thawing (F-T) [2–5]. The maintenance and repair costs of concrete member are usually high.

Surface scaling of concrete caused by the F-T cycles indicates that cement pastes and even fine aggregates are removed from the concrete surface, exposing coarse aggregates [5]. Harmful substances, such as chloride ions, can more easily migrate into the concrete, further increasing the risk of steel corrosion [6]. Previous studies clarified that the surface scaling of concrete under F-T cycles is related to the deformation of the matrix [7]. In contrast, the internal damage is associated with microcracks induced by the F-T cycle within the concrete. In moderate to severe cases of internal damage, the strength and stiffness of the concrete can decreased, causing

* Corresponding author.
E-mail address: wangzhendi@cbmamail.com.cn (Z. Wang).

https://doi.org/10.1016/j.jobe.2025.113604
Received 4 April 2025; Received in revised form 13 July 2025; Accepted 26 July 2025
Available online 28 July 2025

deterioration of concrete structures [8]. Additional concrete reinforcement technology must be considered to ensure the safety of concrete structures [9–11]. Therefore, improving the durability of concrete subjected to cyclic F-T with deicing salt is of great social and economic significance.

In the most widely used standards for assessing frost resistance of concrete, such as ASTM C666 [12], ASTM C672 [13], CEN/TS 12390-9 [14], and RILEM CIF [15], concrete specimens are tested under unrestrained conditions, wherein they remain isolated and can deform freely throughout the entire test process. In contrast, in engineering practices, concrete members are often surrounded by other materials or structures, which restrict the deformation of concrete during cyclic freezing and thawing. Consequently, there is a disparity between current laboratory investigations and the actual service conditions of concrete.

In order to investigate this difference, in 2014, M. Setzer [16] developed a patented concrete restraint device based on the CIF [15] test. Several restraint anchors were used to limit the deformation of concrete during single-side salt freezing and thawing (SSFT) tests. However, Setzer did not conducted further research on the frost damage of concrete in the restrained state.

Since 2016, similar studies have been carried out by Xu [17] and Gao [18]. In their studies, a restraint device using a restraint ring and restraint anchors to restrict expansion and shrinkage deformation was designed [17,18]. SSFT tests on restrained concrete were performed based on the designed restraint device. According to the studies [17,19,20], the restrained concrete exhibited more sever surface scaling but less internal damage than unrestrained concrete. The more severe surface scaling of restrained concrete induced by SSFT has been confirmed to be related to the significant deformation differences between ice and concrete [18]. However, the mechanism for the less internal damage of restrained concrete induced by SSFT remains unclear. Similarly, Hasholt [21] also confirmed that using two hose clamps to restrict the expansion deformation of concrete can reduce the frost microcracks in concrete. These results indicate that the current standard SSFT method may overestimate the internal damage of concrete in engineering practice. It is necessary to clarify the mechanism for internal damage of concrete subjected to SSFT to extend the service life of concrete in cold regions.

The classical theory holds that the frost damage of concrete with pure water is related to water migration and phase transformation inside the concrete. Powers [22]confirmed that the frozen water in the capillary pores of concrete would drive the migration of unfrozen water. As a result, the hydrostatic pressure could damage the concrete matrix. However, the hydrostatic pressure theory is only valid when the concrete is highly saturated [23]. Further research [24] found that the concentration difference and vapor pressure difference of concrete pore solution control the freezing sequence inside the concrete, driving the migration of water from small pores to large pores. Thus, water migration results in osmotic pressure induced frost damage to concrete. The critical saturation theory [25] suggested that saturation of concrete can characterize the water migration and phase transition inside concrete subjected to freezing and thawing. The actual saturation of concrete is related to frost damage, which can be used to predict the frost resistance of concrete. Meanwhile, pore damage in concrete under freeze-thaw action cannot be ignored [26]. The crystallization of water in pores not only attracts the surrounding unfrozen water to migrate towards the ice crystals, but also causes the growing ice crystals to compress the pore walls. Therefore, the growing ice crystals induce pore size expansion and initiate microcracks that propagate from the pore walls to the concrete matrix. Similar experimental results have been reported in previous studies [27]. It can be seen that concrete frost damage is related to water migration and phase transformation inside the concrete, which are affected by temperature and pores.

The internal damage of concrete under SSFT cycles is different from that under pure water F-T cycles. On the one hand, the deformation of concrete subjected to SSFT is manifested as matrix shrinkage during the cooling process and matrix expansion during the heating process [19,20]. The significant breakthrough in calculating the stress of solution migration and phase change explains the above behavior. Setzer clarified the stress caused by solution migration in concrete [28], and the matrix shrinkage was caused by the migration of the solution in the pore. The thermodynamic equilibrium state of moisture changes the water migration of gel pores, capillary pores and the external environment [29], leading to the “pumping absorption” of concrete. The macroscopic manifestation of the concrete matrix is shrinkage during the cooling process and the expansion during the heating process. As a result, the saturation of concrete is increased. Even concrete specimens with a saturation less than 91 % will still experience frost damage [30]. Penttala [31] proposed three macroscopic models of freezing stress for pore solution, which can easily calculate the crystallization stress of the pore solution. Meanwhile, the relative humidity and temperature inside the concrete were taken into consideration as easily obtainable parameters.

On the other hand, the influence of salt solution on water migration and phase transition inside concrete is complex. Previous studies have shown [32–34] that salt solutions can increase the saturation degree and speed of concrete, and a 2 wt% to 6 wt% NaCl solution can exert greater freezing pressure to concrete. Based on the above-mentioned classic theories, a substantial amount of research on the internal damage of unrestrained concrete focused on pore structure [35–38], microcracks [39,40], relative humidity [41], saturation degree [34], and air content [36,42].

However, the only difference between restrained and unrestrained concrete during SSFT cycles is the presence of restraint. The significant difference in the internal damage of restrained and unrestrained concrete subjected to SSFT cycles cannot be explained by the classical theory. Gao [43] compared the evolution of relative humidity inside restrained and unrestrained concrete subjected to SSFT cycles. The results showed that the restraint weakened the internal water migration of the restrained concrete during the test. Furthermore, the impact of restraint on the deterioration of pores inside frozen concrete with deicing salt also deserves investigation.

This study aims to clarify the influence of restraint on the deterioration of pores inside concrete subjected to SSFT cycles. The water-to-cement ratios (W/C) of concrete specimens were 0.60. The internal relative humidity (IRH) and the strain of concrete were continuously monitored during the SSFT cycles. The IRH increment and residual strain of the restrained and unrestrained concrete were compared. A simplified pore structure model was established to calculate the strain due to pore deterioration. The influence mechanism of restraint on internal damage of concrete subjected to SSFT cycles was clarified. The results can provide theoretical guidance for the mix design of high frost resistant concrete in cold regions.

2. Experiment

2.1. Materials and mix ratio

The chemical composition of P. I 42.5 cement used was tested in accordance with GB/T 176–2017 [44], as shown in Table 1. The physical properties of the P. I 42.5 cement used was tested in accordance with GB/T 8074-2008 [45], GB/T 1346–2024 [46], and GB/T 17671-2021 [47], as shown in Table 2. The fine aggregate was natural river sand with a fineness modulus of 2.68, tested in accordance with GB/T 14684-2022 [48]. The coarse aggregate was graded stone, prepared by uniformly mixing crushed stone of 5 mm–10 mm and 10 mm–20 mm in a mass ratio of 4: 6. The mix, 28 days compressive strength and elastic modulus of concrete with a water to cement ratio (W/C) of 0.60 is listed in Table 3. In Table 3, N60R and N60 represent restrained and unrestrained concrete, respectively. The 28 d compressive strength and elastic modulus of concrete were tested in accordance with GB/T 50081-2019 [49].

2.2. Mould and specimens preparation

2.2.1. Concrete mould

The restrained concrete specimens were formed using the restraint device described in reference [18]. The unrestrained concrete specimens were formed using plastic moulds conforming to the provisions of JG 237–2008 [50]. Two groups of specimens were prepared: restrained concrete specimens (N60R) and unrestrained concrete specimens (N60), with five specimens in each group. These specimens were used for IRH monitoring and concrete strain monitoring, respectively.

(1) Moulds for restrained concrete specimens

The mould and restraint device for forming the restrained concrete specimens are shown in Fig. 1.

The device in Fig. 1a served both as the mould for casting a restrained concrete specimen and as the restraining device to limit concrete deformation during SSFT cycles. The device consisted of a restraint ring, 24 restraint anchors, a counter-force ring, and a flange. All parts of the device were made of 304 stainless steel. The design parameters of the restraint device are shown in Fig. 1b.

The restraint ring had a thickness of 8 mm, an inner diameter of 100 mm, and a height of 70 mm. The restraint ring and the flange formed the mould for casting the restrained concrete specimen. The restraint ring provided expansion restraint stress for the hardened concrete to limit its expansion deformation during the SSFT test. When the thickness of the restraint ring increased from 1 mm to 4 mm and 8 mm, the expansion restraint stress increased by 280 % and 410 %, respectively [51].

The 24 steel anchors, each with a diameter of 6 mm, were mounted on the restraint ring in three vertical direction. That is, 8 anchors were evenly distributed in each layer along the restraint ring. One end of the anchors was embedded 28 mm into the concrete during casting, and the other end was fixed by hexagonal nuts on the outermost counter-force ring during the SSFT tests. All the steel anchors point to warded the axis of the restraint ring. The anchors provided shrinkage restraint stress for the hardened concrete to limit its shrinkage deformation during the SSFT test. When the embedded length of the anchors increased from 28 mm to 33 mm, the shrinkage restraint stress increased by 26 % [51].

The counterforce ring had a thickness of 4 mm and a height of 70 mm. It was a steel ring composed of 8 steel arc plates connected by bolts and was located on the outermost side of the restraint device. Before the concrete casting, the counterforce ring was used to fix the steel anchors. During the SSFT test, it provided the counter force for the steel anchors.

The flange was a circular flat steel plate connected to the restraint ring by removable bolts. After the concrete hardens, the flange was removed, and the bottom surface of the hardened concrete, which is in contact with the flange, will be used as the test surface for the SSFT test.

As shown in Fig. 1b, in this study, a restraint combination consisting of a restraint ring with a thickness of 8 mm and 24 steel anchors with an embedded length of 28 mm in concrete was used. The restraint ring and steel anchors were not fixed.

(2) Moulds for unrestrained concrete specimens

The unrestrained concrete specimens were formed using plastic cylindrical moulds, as shown in Fig. 2. The inner diameter of the mould was 100 mm, and the height was 70 mm. The size of the unrestrained concrete specimens was consistent with that of the restrained concrete specimens.

2.2.2. Specimens preparation

The specimens were prepared according to the CIF test [15] and GB/T 50082-2024 [52], as shown in Fig. 3.

The fresh concrete was cast into the restraint ring and plastic cylindrical moulds (no release agent was applied to the moulds),

Table 1
Chemical composition of cement (wt./%).

SiO_2	Al_2O_3	Fe_2O_3	CaO	MgO	SO_3	$Na_2Oeq.$	Loss	f-CaO
25.1	6.38	4.19	54.87	2.61	2.66	0.56	2.18	0.79

Table 2
Physical properties of cement.

Specific surface/$m^2 \cdot kg^{-1}$	Water demand/%	Setting time/min		Flexural strength/MPa		Compressive strength/MPa	
		initial	final	3d	28d	3d	28d
346	24	169	253	4.0	7.3	25.1	54.0

Table 3
Concrete mix and properties.

No.	Cement/$kg \cdot m^{-3}$	Water/$kg \cdot m^{-3}$	W/C	Gravel/$kg \cdot m^{-3}$	Sand/$kg \cdot m^{-3}$	28 d compressive strength/MPa	28 d elastic modulus/GPa
N60R, N60	360	216	0.60	1045	810	33.2	23.84

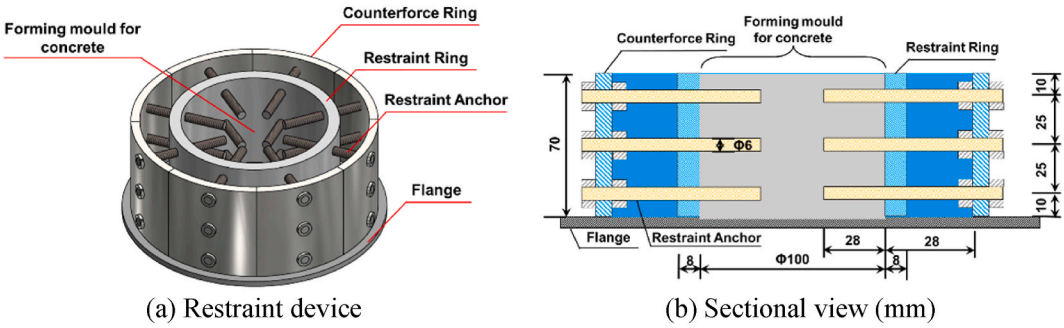

Fig. 1. Sketch of mould and restraint device for restraint concrete [43].

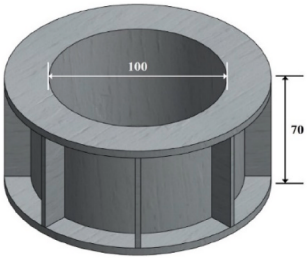

Fig. 2. Sketch of the plastic forming mould (mm).

respectively. After vibration, the upper surface of the specimen was troweled. All the specimens were cured in air at (50 ± 5)% relative humidity (RH), and (20 ± 2)°C for 1 d (Fig. 3a).

The restrained concrete was obtained by removing the flange of the restraint device (Fig. 4a). The unrestrained concrete was obtained by removing the plastic cylindrical mould with compressed air (Fig. 4b). The test surfaces of the two types of concrete used in the SSFT test were the surfaces opposite to the troweled surface.

The specimens were placed in water at (20 ± 2)°C for curing for 6 days (Fig. 3b). Then, the they were moved to air at (65 ± 5)% RH, and (20 ± 2)°C for curing until the age of 25 days (Fig. 3c). All sides of the specimen except the test surface were sealed with aluminum foil (Fig. 3d). Subsequently, the specimens were cured in air at (65 ± 5)% RH, and (20 ± 2)°C until the age to 28 days.

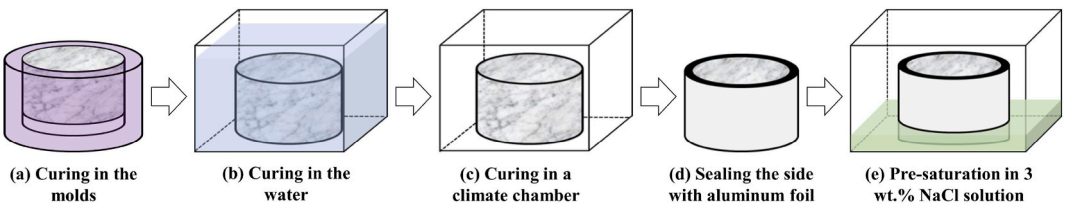

Fig. 3. Curing and pre-saturation process of concrete specimen.

(a) Restrained concrete specimen (b) Unrestrained concrete specimen

Fig. 4. Specimens of restrained concrete and unrestrained concrete.

The specimens were pre-saturated in 3 wt% NaCl solution at (20 ± 2)°C for 7 days. During pre-saturation, the test surface of the specimen was facing downward, and the liquid level was (10 ± 1) mm higher than the test surface of the specimen. The SSFT cycles began after the specimens were pre-saturated.

2.3. Test method

In order to investigate the effect of restraint on salt frost damage of concrete, the internal relative humidity, temperature, and strain of both restrained and unrestrained concrete were monitored through the SSFT test. The evolution of residual strain in the two types of

(a) Temperature-humidity sensor

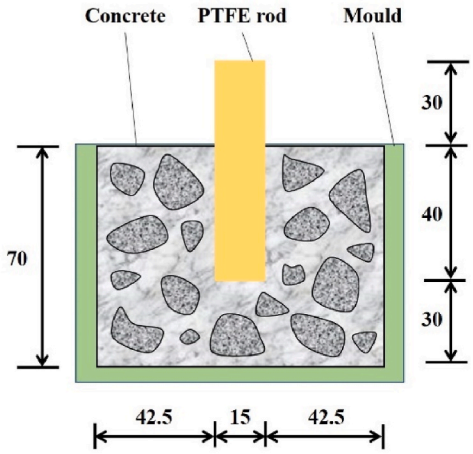

(b) Positioning plastic rod (mm)

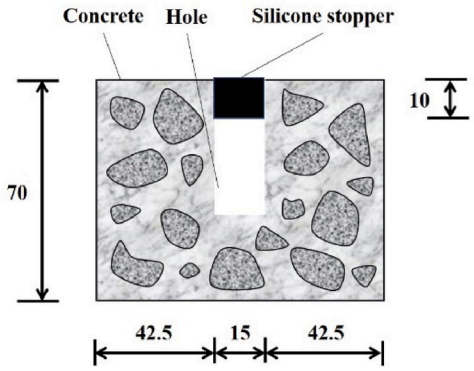

(c) Sealing hole (mm)

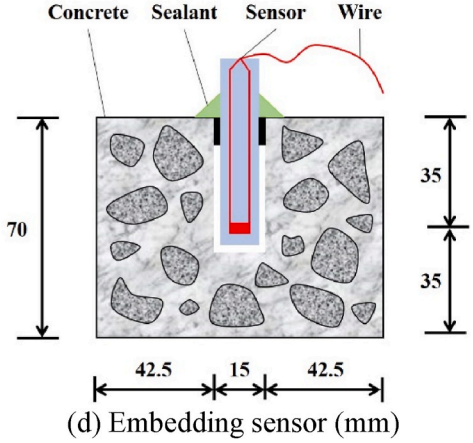

(d) Embedding sensor (mm)

Fig. 5. Preparation before monitoring the internal relative humidity of concrete [43].

concrete was calculated to clarify the effect of restraint on salt frost damage of concrete.

(1) The SSFT test

The CDF/CIF TESTER, produced by Schleibinger Geräte, was used to provide the SSFT cycles. The temperature regime and the test parameters were set according to the CIF test [15] and GB/T 50082-2024 [52]. The number of SSFT cycles were 28. During the test, it was ensured that the test surface of the specimen was facing downward. The liquid level of the 3 wt% NaCl solution was (10 ± 1) mm higher than the test surface of the specimen.

(2) Internal relative humidity and temperature monitoring

A temperature and relative humidity (T-RH) sensor (Fig. 5a) was used to monitor the evolution of internal relative humidity (IRH) and temperature inside the concrete subjected to the SSFT cycles. The accuracy of temperature and relative humidity measured by the T-RH sensor was 0.01 °C and 0.1 %, respectively. The embedding of the T-RH sensor in the concrete is shown in Fig. 5b–d.

A plastic rod with a diameter of 15 mm and a length of 70 mm was embedded during the casting of fresh concrete (Fig. 5b). The plastic rod was pulled out before the final setting of the concrete. A silicone stopper was used to seal the exposed hole (Fig. 5c). The silicone stopper was emptied before the SSFT cycles. The T-RH sensor was inserted into the exposed hole, and a sealant was used to seal the gaps between the T-RH sensor and the hole (Fig. 5d). The above method of embedding the T-RH sensor can ensure that the T-RH sensor probe was located in the center of the concrete specimen. Therefore, the evolution of IRH and temperature of concrete during the SSFT cycle can be obtained.

The NP130T recorder was used to collect data on the evolution of internal relative humidity (IRH) and temperature inside the concrete subjected to the SSFT cycles. The data recording frequency was once per minute.

(3) Strain and residual strain monitoring

The resistance strain gauge and polyvinyl chloride (PVC) flexible glass were used to make a strain sensor (see Fig. 6). The resistance strain gauge used was of type BFH120-50AA, featuring a sensitive grid of 50 mm × 3 mm, a standard resistance value of (120 ± 1) Ω, and a sensitivity of (2.0 ± 1.0)%. The overall dimensions of the resistance strain gauge were 55 mm × 6 mm × 0.1 mm. The accuracy of strain measured by the resistance strain gauge was 0.01 με. The size of the PVC flexible glass was 75 mm × 12 mm × 1.5 mm. Silicone sealant was used as a waterproof coating.

The strain sensor was embedded during the casting of fresh concrete. The position of the strain sensor in the concrete specimen is shown in Fig. 7. Thus, the sensor was located at the center of the vertical height of the concrete specimen. The concrete matrix strain can be monitored by the strain sensor during the SSFT cycles. The TST 3822 EN recorder was used to collect data on the evolution of strain of the concrete subjected to the F-T cycles. The data recording frequency was once per minute. The TST 3822 EN recorder was equipped with temperature compensation to eliminate the influence of thermal deformation on concrete strain.

The residual strain of concrete after the nth cycle was calculated as follows:

$$S_n = \sum_{k=1}^{n} (S_k - S_{k-1}) \tag{1}$$

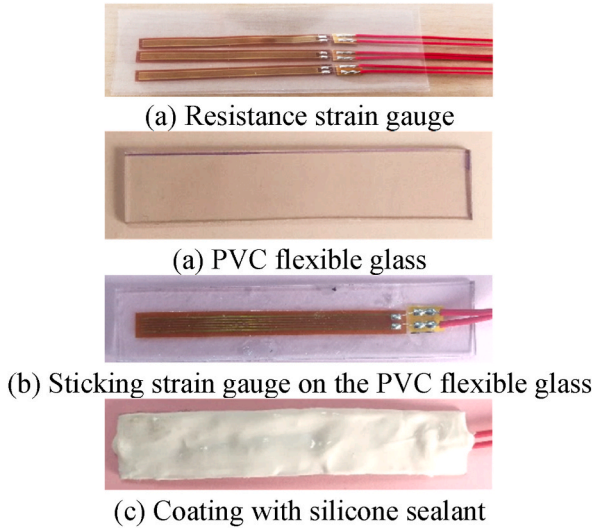

Fig. 6. Preparation of strain sensor.

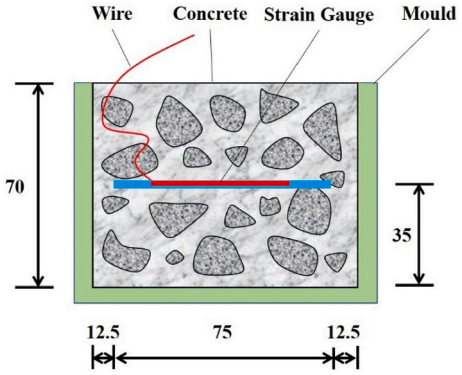

Fig. 7. Position of the strain sensor in concrete specimen (mm).

where,

S_n is the residual strain of concrete after the nth cycle;

S_k is the strain of the concrete at the beginning of the kth cycle;

S_{k-1} is the strain of the concrete at the beginning of the (k-1)th cycle.

3. Results

3.1. Influence of the restraint on the IRH of the concrete

The evolution of the internal relative humidity (IRH) with temperature of concrete specimens (N60R-restained, N60-unrestrained) during the 1st, 16th, and 28th cycles is shown in Fig. 8a and (b).

As shown in Fig. 8, the variation of IRH in each cycle of concrete can be clearly observed. As the temperature starts to drop from 20 °C, the IRH in both restrained and unrestrained concrete decreased rapidly. However, the IRH of restrained and unrestrained concrete increased at −8.7 °C and −9.5 °C, respectively. According to Wang [41], the inflection point of the IRH curve indicates the freezing point of water in concrete. When the temperature is near the freezing point of water, the saturated vapor pressure of water decreases. Water exhibits a"super-cooling" behavior. At this time, there is no ice crystal nucleation in the water, and the water in concrete can still exist in the liquid phase. The saturated vapor pressure of water is higher than that of ice [41]. Unfrozen water is more likely to change from the liquid phase to the gas phase as the temperature drops, which causes the IRH of concrete to increase [43]. The "super-cooling" behavior of water inside concrete is common during the IRH monitoring of concrete subjected to F-T cycles. Similar phenomena have been reported in the studies of Wang [41] and Hou [53].

Furthermore, as the temperature continued to decrease, ice crystals nucleated and grew rapidly in the liquid phase for the first time. The saturated vapor pressure of water decreases significantly, causing water to transform from the gas phase to the liquid phase and then freeze. As a result, the IRH of concrete decreased significantly. The entire process shows that −8.7 °C and −9.5 °C are the freezing points of restrained and unrestrained concrete, respectively.

Moreover, the IRH of concrete further decreased during the isothermal process at −20 °C. During the heating process, the IRH of

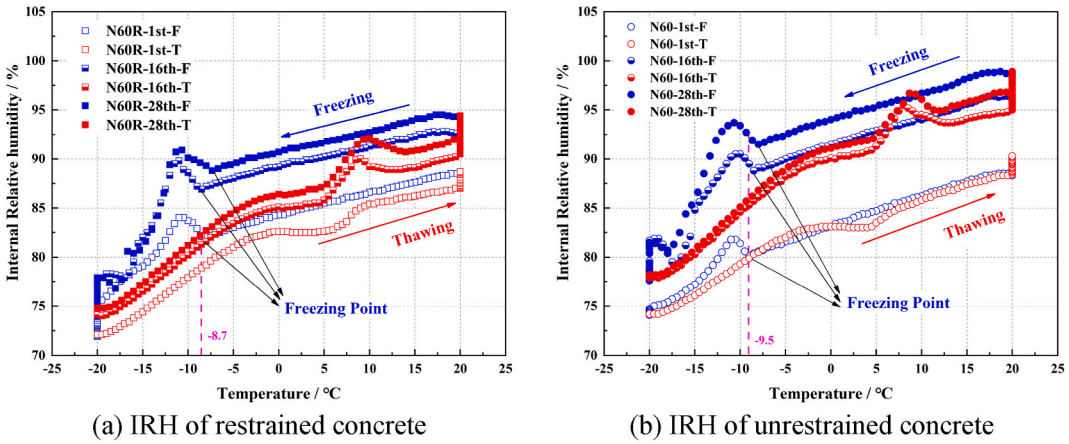

Fig. 8. Curve of IRH–temperature of restrained and unrestrained concrete.

concrete increased. It was worth noting that the IRH of concrete increased after each F-T cycle, resulting in obvious hysteresis in the IRH–temperature curves of both restrained and unrestrained concrete. Fig. 9 shows the IRH increment of restrained and unrestrained concrete after every 4 F-T cycles.

The IRH increment of concrete increased with the number of F-T cycles. After the 28th F-T cycles, the IRH increment of restrained concrete was 30 % less than that of unrestrained concrete. Thus, the hysteresis in the IRH–temperature curves of unrestrained concrete was more significant than that of restrained concrete, which may be related to the difference in internal damage between restrained and unrestrained concrete induced by F-T cycles.

3.2. *Influence of the restraint on the strain of the concrete*

The evolution of strain with temperature for concrete specimens (N60R and N60) during the 1st, 16th, and 28th cycles is shown in Fig. 10a and (b).

In Fig. 10, the evolution of concrete strain in each cycle is similar to that of the IRH. As the temperature began to drop from 20 °C, the strain of both restrained and unrestrained concrete decreased rapidly. The strain of restrained and unrestrained concrete started to decrease at −8.7 °C and −9.5 °C, respectively, which is different from the behavior of IRH. Previous studies [26,28] have indicated that the shrinkage of pores is related to water migration in pores. The mechanism is similar to the matrix deformation induced by drying shrinkage. In Fig. 8, water shows “super-cooling” behavior inside restrained and unrestrained concrete at −8.7 °C and −9.5 °C, respectively. Unfrozen water easily migrated as a gas phase from gel pores to macropores and capillary pores. Gel pores shrank due to the water loss, leading to significant matrix shrinkage at the freezing point. Similar phenomena have been reported in the studies of Zeng [36] and Wang [54].

As the temperature further decreased, the strain change of restrained concrete is more slightly than that of unrestrained concrete. The result indicates that the restraint has a significant impact on the deformation of concrete. A previous study [43] confirmed that due to the restraint device, water migration in restrained concrete is weakened during the cooling process. Accordingly, it is difficult for unfrozen water to migrate towards ice crystals in restrained concrete. On the contrary, the migration of unfrozen water towards ice crystals in unrestrained concrete is significant [28]. The difference in pore size between restrained and unrestrained concrete during the cooling process also supports this mechanism [43].

During the isothermal process at −20 °C, the strain of both restrained and unrestrained concrete increased rapidly. The result shows that the concrete matrix expands, which is related to the formation of ice crystals within the pores. Previous studies [26,28] have confirmed that the formation of ice crystals within the pores can push the pore wall. As a result, the tensile stress can be initiated on the pore walls, marking the beginning of frost damage to concrete.

When the heating process began, the concrete strain further increased, indicating that ice crystals were still pushing the pore walls. Accordingly, the pore walls were still under tensile stress. As the temperature further increased, the melting temperature of frozen water inside the pore is related to the pore size [24]. Ice in smaller pores melted first, releasing the stress on the pore walls. Meanwhile, ice crystals prevented water from migrating to gel pores. Accordingly, gel pores can only absorb water from the outside, resulting in further expansion of the matrix.

During the heating process, it is difficult to determine the exact melting point of water in concrete [41]. However, it can be confirmed that the strain of both restrained and unrestrained concrete begins to decrease at around 10 °C. The result indicates that the ice in macropores melts, leading to a significantly release of stress on the pore walls. Although gel pores still absorb water from the outside, the matrix shrinks slightly. The shrinkage of the matrix can continue until the end of the isothermal process at 20 °C. It is worth noting that the strain of concrete does not return to the initial value, indicating that the deformation of concrete induced by F-T cycles

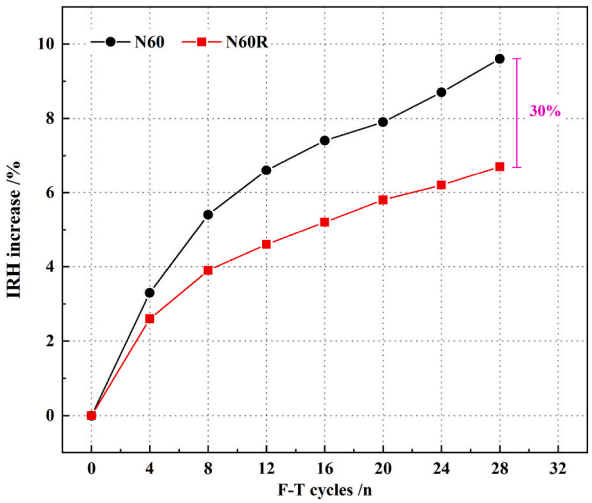

Fig. 9. IRH increment of restrained and unrestrained concrete subjected to SSFT cycles.

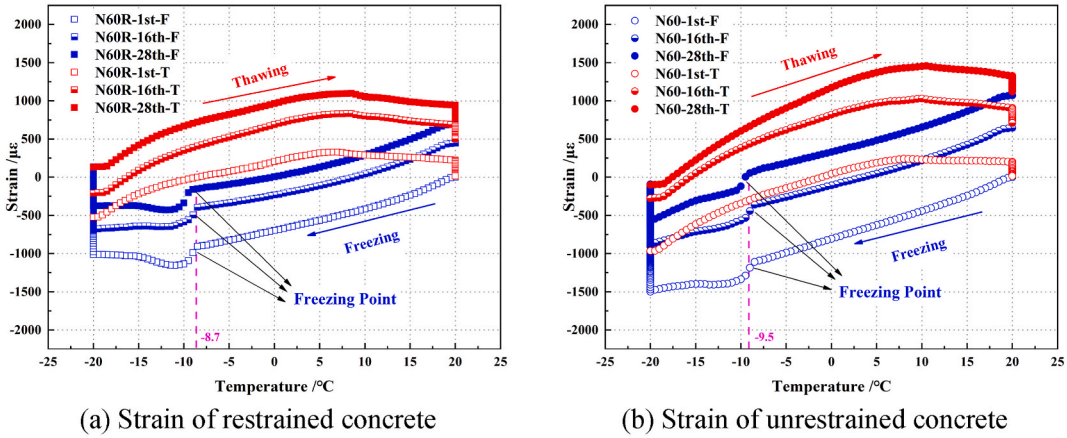

Fig. 10. Curve of strain–temperature of restrained and unrestrained concrete.

cannot be fully restored. The obvious hysteresis of concrete strain is similar to that of the IRH, leading to the residual strain of concrete shown in Fig. 11.

As shown in Fig. 11, the concrete strain increases with the number of F-T cycles, which is related to the initiation of microcracks inside the concrete induced by F-T cycles [27]. After the 4th F-T cycle, there was no significant difference in residual strain between restrained and unrestrained concrete. In the early stage of the test, the damage to the pore walls caused by ice crystals was low, and the internal damage of concrete induced by F-T cycles was not significant. A similar phenomenon has also been described in Ref. [20]. After 28 F-T cycles, the S_n (residual strain) of restrained concrete was 30 % less than that of unrestrained concrete. The results indicate that the restraint significantly reduces the internal damage of concrete subjected to F-T cycles, which is consistent with the results of previous studies [17,20,51]. Consequently, the hysteresis in the strain–temperature curves is more pronounced in unrestrained concrete than in restrained concrete (Fig. 10).

Prior research has associated greater residual strain with more internal concrete damage [54]. However, the mix proportions of restrained and unrestrained concrete were exactly the same. The difference in internal damage may be related to the restraint. In addition, the pictures of the specimens' test surface after 28 SSFT cycles are shown in Fig. 12.

As shown in Fig. 12a, coarse aggregates were already exposed on the test surface of the restrained concrete, whereas no obvious coarse aggregate exposure was observed on the test surface of the unrestrained concrete (Fig. 12b). The results indicates that surface scaling of the restrained concrete is more severe than that of the unrestrained concrete after 28 SSFT cycles. Similar phenomena have been reported [17,19,20]. A previous study [18] clarifies that the more severe surface scaling of restrained concrete induced by SSFT cycles is related to the deformation mismatch between the concrete and ice layer. However, the mechanism by which restraint reduces the internal damage of concrete subjected to SSFT cycles remains unclear. Further discussion of the impact mechanism of restraint on internal damage is crucial.

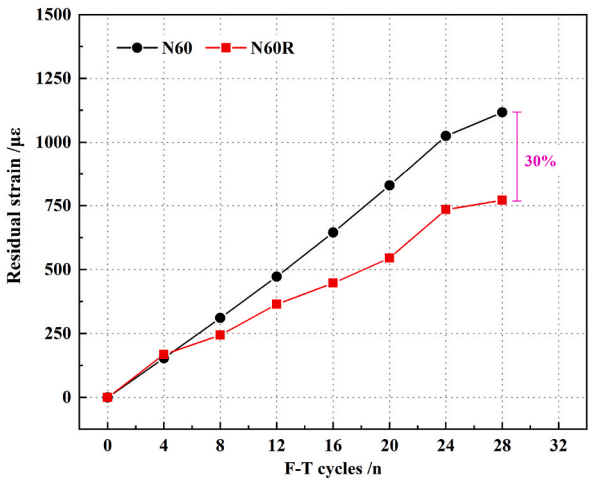

Fig. 11. Residual strain of restrained and unrestrained concrete subjected to SSFT cycles.

(a) Restrained concrete specimen (b) Unrestrained concrete specimen

Fig. 12. Images of the test surface of restrained and unrestrained concrete after 28 SSFT cycles.

4. Discussion

4.1. Interrelation between deformation and frost damage in concrete

According to previous research [26,29], water migration and phase transformation inside concrete induced by freeze – thaw (F-T) cycles are significant. The results in Figs. 8–11 also provide evidence for water migration and phase transformation. The Crystallization Pressure theory [26] posits that the frost damage of porous materials originates from the deterioration of the pore structure, particularly during the cooling process. Ice crystals in pores may grow along both the radial and axial directions of the pore. Simultaneously, unfrozen water migrates from gel pores to ice crystals, causing the pore wall to shrink [28]. As a results, tensile stress is generated on the pore wall, which may lead to the initiation of microcracks, as shown in Fig. 13.

The Crystallization Pressure theory assumes that the pores in porous materials are all spherical or cylindrical. Two important equations are proposed for calculating the stress on the pore wall during the cooling process, as shown in Eq. (1) and Eq. (2).

$$p_{SA} = p_L + 2\gamma_{CL}\left(\frac{1}{r_E} - \frac{1}{r_p}\right) \tag{1}$$

$$p_{CA} = p_L + \frac{\gamma_{CL}}{r_p} \tag{2}$$

where,

p_{SA} is the stress on the spherical pore wall, in MPa;
p_L is the stress on the pore wall induced by water migration, in MPa;
γ_{CL} is the interface energy of the ice-water interface, in J·mm^{-2};
r_E is the radius of the spherical pore for growing ice crystals;

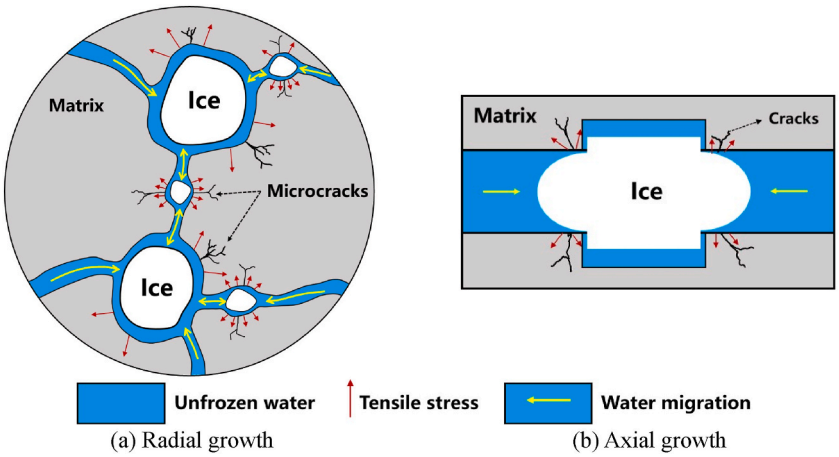

Fig. 13. Growth direction of ice crystals in pore.

r_p is the radius of the cylindrical pore for growing ice crystals;
p_{CA} is the stress on the cylindrical pore wall, in MPa.

The calculation of the stress on the pore wall using the Crystallization Pressure theory depends on the pore shape. Meanwhile, the calculation of the stress induced by water migration (p_L) also requires assumptions about the pore size [55]. Consequently, there is a significant difference in the calculation results of the stresses on the walls of spherical and cylindrical pores [56].

However, it is challenging to clarify all the sizes and shapes of pores inside concrete under existing experimental conditions. In order to address this issue, Setzer provided a model for calculating the shrinkage stress of water migration on the pore wall based on thermodynamic, as shown in Eq. (3).

$$\Delta p_t = 1.2225(T - T_0)\left[1000 + 3.25(T - T_0) - 0.016(T - T_0)^2\right] \times 10^{-3} \tag{3}$$

where,
Δp_t is the shrinkage stress of water migration on the pore wall, in MPa;
T is the current temperature, in K;
T_0 is the baseline temperature, in K.

Furthermore, Penttala [31] proposed a theoretical model for the expansion stress on the pore wall induced by phase transformation of water. The model calculates the expansion stress based on the temperature of the concrete during the freezing process (the test temperature in the literature [31] is 20 °C ~ −70 °C) and the internal relative humidity (IRH), as shown in Eq. (4) ~ Eq. (7).

$$\Delta p_f = \frac{RT}{\nu_i}\ln\left(\frac{p_v}{p_0}\right) + \frac{h^{\circ}_{wi}}{\nu_i T_0}(T - T_0) + \frac{1}{\nu_i}\int_{T_0}^{T}\int_{T_0}^{T}\frac{c^{\circ}_{pi}(T) - c^{\circ}_{pw}(T)}{T}dTdT \tag{4}$$

$$\mathrm{IRH} = \frac{p_v}{p_0} \tag{5}$$

$$c^{\circ}_{pi}(T) = 38.052\left[1 + 373.7 \times 10^{-5} \times (T - T_0)\right] \tag{6}$$

$$c^{\circ}_{pw}(T) = 75.996\left[1 - 54.0 \times 10^{-5} \times (T - T_0)\right] \tag{7}$$

where.

Δp_f is the expansion stress on the pore wall, in MPa;
R is the standard gas constant, 8.314 J mol^{-1} K^{-1};
ν_i is the specific volume of ice, 1.998 × 10^{-5} m^3 mol^{-1} [31];
p_v is the vapor pressure of pore water, in MPa;
p_0 is the saturated vapor pressure of pore water, in MPa;
h°_{wi} is the freezing heat of water at 273.15 K, 6 × 10^3 J mol^{-1} [31];
$c^{\circ}_{pi}(T)$ is the specific heat capacity of ice, in J·mol^{-1};
$c^{\circ}_{pw}(T)$ is the specific heat capacity of water, in J·mol^{-1}.

The pores will deform or even deteriorate under the action of the above mentioned shrinkage and expansion stresses. Consequently, the expansion of pore size and the initiation of microcracks are both manifestations of concrete frost damage [20,27,51,57]. Meanwhile, the deformation of concrete matrix induced by F-T cycle is a macroscopic manifestation of pore deterioration [26,29]. Therefore, an interrelation between deformation and frost damage in concrete can be established based on pore deterioration.

Accordingly, the concrete matrix, including cement mortar and aggregates, without pores can be assumed to be dense. Therefore, the dense matrix only undergoes thermal deformation during F-T cycles. Here a simplified equation can be established based on the assumption that the deformation of concrete induced by F-T cycles consisted of the following components: thermal deformation (including thermal expansion and shrinkage) and pore deformation. The deformation of the pore wall includes pore wall expansion, pore wall shrinkage, and pore wall deterioration. Strain can be used to quantitatively characterize the above-mentioned deformations, as shown in Eq. (8).

$$\varepsilon = \varepsilon_T + \varepsilon_f + \varepsilon_t + \varepsilon_p \tag{8}$$

where,
ε is the total strain of concrete;
ε_T is the thermal strain of concrete;
ε_f is the expansion strain on the pore wall induced by phase transformation of water;
ε_t is the shrinkage strain on the pore wall induced by water migration;
ε_p is the strain due to the pore deterioration.

There is no doubt that the models from Setzer and Penttala ignore the pore parameters, which is beneficial for further analysis and discussion. However, due to the difference between the deformation and stress, it is difficult to directly apply these models. A more

suitable model needs to be established to evaluate the pore deterioration in restrained and unrestrained concrete subjected to SSFT cycles.

4.2. Simplified model of concrete pore and strain on the pore wall

The pores inside concrete are surrounded by hardened cement mortar [58]. The pore size is much smaller than the thickness of hardened cement mortar. Thus, a thick-walled cylindrical model with infinite outer diameter and finite inner diameter is established to represent the pore inside concrete, as shown in Fig. 14.

According to the Lamè equation [59], the circumferential, radial, and axial stresses at point A ($R_i < r < R_o$) can be calculated by Eq. (9)–(15).

$$G = \frac{R_0}{R_i} \tag{9}$$

$$\sigma_\theta = \frac{p_i}{G^2 - 1}\left(1 + \frac{{R_0}^2}{r^2}\right) \tag{10}$$

$$\sigma_r = \frac{p_i}{G^2 - 1}\left(1 - \frac{{R_0}^2}{r^2}\right) \tag{11}$$

$$\sigma_z = \frac{p_i}{G^2 - 1} \tag{12}$$

$$\sigma_\theta{}' = \frac{-p_i{}'K^2}{G^2 - 1}\left(1 + \frac{{R_i}^2}{r^2}\right) \tag{13}$$

$$\sigma_r{}' = \frac{-p_i{}'G^2}{G^2 - 1}\left(1 - \frac{{R_i}^2}{r^2}\right) \tag{14}$$

$$\sigma_z{}' = -\frac{G^2}{G^2 - 1}p_i{}' \tag{15}$$

where,

G is the cylinder thickness characteristics;
R_0 is the outer radius of the model, mm;
R_i is the inner radius of the model, mm;
r is the distance from the axis of the cylinder to point A, in mm, and $R_i < r < R_0$;
σ_θ is the circumferential tensile stress at point A, in MPa;
σ_r is the radial tensile stress at point A, in MPa;
σ_z is the axial tensile stress at point A, in MPa;
$\sigma_\theta{}'$ is the circumferential compressive stress at point A, in MPa;
$\sigma_r{}'$ is the radial compressive stress at point A, in MPa;

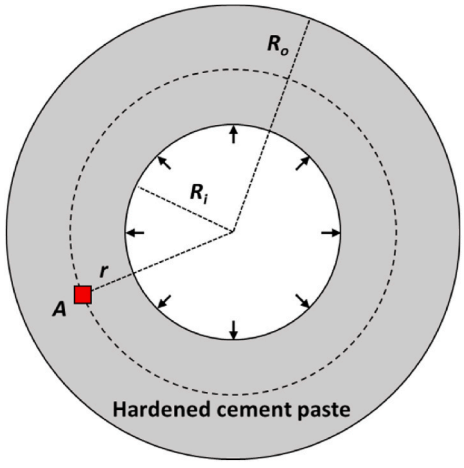

Fig. 14. Sketch of stress at pore wall based on the proposed thick-walled cylinder model.

σ_z' is the axial compressive stress at point A, in MPa;
p_i is the stress acting on the inner wall of the model, directed towards the inner wall, in MPa;
p_i' is the stress acting on the inner wall of the model, directed towards the axis, in MPa.

When point A is located on the inner wall of the thick-walled cylinder model, the condition "$r = R_i$" is obtained. Therefore, Eq. (10), Eq. (11), Eq. (13), and Eq. (14) can be simplified to Eq. (16) to Eq. (19).

$$\sigma_\theta = \frac{G^2+1}{G^2-1} p_i \tag{16}$$

$$\sigma_r = -p_i \tag{17}$$

$$\sigma_\theta' = -\frac{2G^2}{G^2-1} p_i \tag{18}$$

$$\sigma_r = 0 \tag{19}$$

According to the generalized Hooke's law [60], the circumferential tensile strain and circumferential compressive strain on the inner wall of thick-walled cylinder model can be calculated by Eq. (20) and Eq. (21), respectively.

$$\varepsilon_\theta = \frac{1}{E}[\sigma_\theta - \mu(\sigma_r + \sigma_z)] \tag{20}$$

$$\varepsilon_\theta' = \frac{1}{E}[\sigma_\theta' - \mu(\sigma_r' + \sigma_z')] \tag{21}$$

where,

ε_θ is the circumferential tensile strain on the inner wall of thick-walled cylinder model;
ε_θ' is the circumferential compressive strain on the inner wall of thick-walled cylinder model;
E is the elastic modulus of the materials, in MPa;
μ is the Poisson's ratio of the materials.

Substituting Eq. (12), Eq. (15), Eq. (16)– (19) into Eq. (20) and Eq. (21) yields the calculation method of the circumferential strain on the inner wall of the cylinder, as shown in Eq. (22) and Eq. (23).

$$\varepsilon_\theta = \frac{p_i}{E} \cdot \frac{(1+\mu)G^2 + 1 - 2\mu}{G^2-1} \tag{22}$$

$$\varepsilon_\theta' = \frac{p_i}{E} \cdot \frac{(\mu-2)G^2}{G^2-1} \tag{23}$$

For concrete, since the pore size is much smaller than the thickness of the hardened cement paste, that is, $r \gg R_i$, it is easy to obtain that the cylinder thickness characteristics tends to infinity. Thus, Eq. (22) and Eq. (23) can be further simplified to Eq. (24) and Eq. (25).

$$\varepsilon_\theta = (1+\mu)\frac{p_i}{E} \tag{24}$$

$$\varepsilon_\theta' = (\mu-2)\frac{p_i'}{E} \tag{25}$$

The circumferential strain on the pore wall in the above equations is independent of the pore size, which is significant for the study of pore deterioration in concrete subjected to SSFT cycles. Furthermore, Eq. (3) and Eq. (4) can be introduced into Eq. (25) and Eq. (24) to obtain the shrinkage and expansion strains of pores induced by water migration and phase transformation, respectively, as shown in Eq. (26) and Eq. (27).

$$\varepsilon_t = (\mu-2)\frac{\Delta p_t}{E} \tag{26}$$

$$\varepsilon_f = (1+\mu)\frac{\Delta p_f}{E} \tag{27}$$

4.3. Influence of the restraint on the deterioration of the pores

Based on the discussion in 4.1 and 4.2, the strain due to the pore deterioration (ε_p) inside concrete induced by SSFT can be calculated according to Eq. (8), Eq. (26), and Eq. (27), as shown in Eq. (28).

$$\varepsilon_p = (\varepsilon - \varepsilon_T) - \left[(1+\mu)\frac{\Delta p_f}{E} + (\mu-2)\frac{\Delta p_t}{E}\right] \tag{28}$$

In this study, the thermal strain of concrete has been eliminated through the temperature compensation function of the TST 3822 EN recorder. According to Figs. 8 and 10, the freezing points of water inside restrained and unrestrained concrete are approximate −8.7 °C and −9.5 °C, respectively. For analysis, the calculation temperature range of the ε_p is from −8.7 °C in the cooling stage to −8.7 °C in the heating process in one cycle. The values of the parameters required for the calculation are presented in Table 4.

Incorporating the values of the parameters in Table 4 into Eq. (28), the strain due to pore deterioration can be calculated. The results are shown in Fig. 15.

As shown in Fig. 15, the ε_p curve shows significant stage characteristics. During the cooling process from the freezing point to −20 °C, ε_p of restrained and unrestrained concrete is positive and increases with the temperature decreasing. The results indicate that tensile strain occurs on the pore wall. Meanwhile, ε_p of restrained concrete is always less than that of unrestrained concrete. The least square method is used for linear fitting. The slope of the fitting line represents the change rate of ε_p. The change rate of the tensile strain on the pore wall of restrained concrete is 11 % less than that of unrestrained concrete, indicating that the growth of ice crystals in pores inside restrained concrete is slower. The weak water migration in restrained concrete before the freezing point results in less frozen water in the pores [43]. In contrast, the intense water migration inside unrestrained concrete promotes further growth of ice crystals in the pores.

During the isothermal process at −20 °C, ε_p of restrained and unrestrained concrete continues to increase. However, the difference in the change rate of the ε_p is slight (about 3.5 %), indicating that the water in the pores of restrained and unrestrained concrete continues to freeze. The results shows that the effect of water migration on ε_p is slight, which is related to ice crystal hindering further water migration [30]. Subsequently, ε_p of both restrained and unrestrained concrete increases significantly. The results indicate that the tensile stress on the hole wall is significantly increased by ice crystals growing in the pores. However, ε_p of restrained concrete is 10 % less than that of unrestrained concrete.

Further, with the increasing of time, the ε_p of both restrained and unrestrained concrete gradually increases until it reaches the peak value. In order to counterbalance the tensile stress imposed by ice crystals on the pore wall, the pore wall deforms. This observation is consistent with the expansion of pore size within concrete induced by F-T cycles, as reported in Refs. [20,27,51,57]. The peak value of ε_p in restrained concrete is 18 % less than that in unrestrained concrete. Meanwhile, the deformation of the pore wall in restrained concrete is 55 % less than that in unrestrained concrete.

Notably, once ε_p reaches its peak value, it starts to decrease rapidly, indicating that the pore wall has cracked due to strain. Consequently, the microcracks initiate from the pore wall and propagate towards the matrix, as described in Ref. [26]. From this point on, ε_p decreases substantially in both restrained and unrestrained concrete. When the calculation endpoint is reached, the ε_p of restrained concrete is 30 % less than that of unrestrained concrete.

In general, it is concluded that the restraint significantly influences the internal damage of concrete during the SSFT cycles. The governing behavior is manifested by the slighter pore deterioration:

The evolution of IRH indicates that the hysteresis in the IRH–temperature curves of unrestrained concrete is more significant than that of restrained concrete. The evolution of concrete strain indicates that the restraint reduces deformation of matrix during SSFT cycles by weakening water migration. The strain on the pore wall suggests that potential internal damage of restrained concrete is significantly lower than that of unrestrained concrete.

These results demonstrate that restrained concrete's limited water migration capacity below the freezing point reduces pore wall strain induced by ice crystal growth. Slower ice crystal formation in restrained concrete further mitigates the tensile strain on the pore walls, thereby reducing strain associated with pore deterioration. In conclusion, applying restraint mitigates the internal damage of concrete subjected to SSFT cycles.

5. Conclusion

This paper explores the influence of restraint on the pore deterioration within concrete with a water cement ratio of 0.60 under single-side salt freezing and thawing (SSFT) cycles. The internal relative humidity (IRH) and strain of both restrained and unrestrained concrete were monitored throughout the SSFT cycles. A comparison was made between the increment of IRH and residual strain of the restrained and unrestrained concrete. The difference in strain resulting from pore deterioration between restrained and unrestrained concrete was calculated using the established pore structure model. The conclusions are as follows:

Table 4
Parameters for calculating the strain due to pore deterioration.

Elements	Description	Values or the source of values	Units
$\varepsilon - \varepsilon_T$	Concrete strain without thermal strain	Measured in the 28th F-T cycles	με
IRH	Internal relative humidity	Measured in the 28th F-T cycles	%
μ	Poisson's ratio of concrete [61]	0.2	/
E	Elastic modulus of concrete	23.84	GPa
ν_i	Specific volume of ice	1.998×10^{-5}	$m^3 \cdot mol^{-1}$
h°_{wi}	Freezing heat of the water at 273.15 K	6×10^3	$J \cdot mol^{-1}$
T_0	Reference temperature	273.15	K
T	Current temperature	Measured during the F-T cycles	K

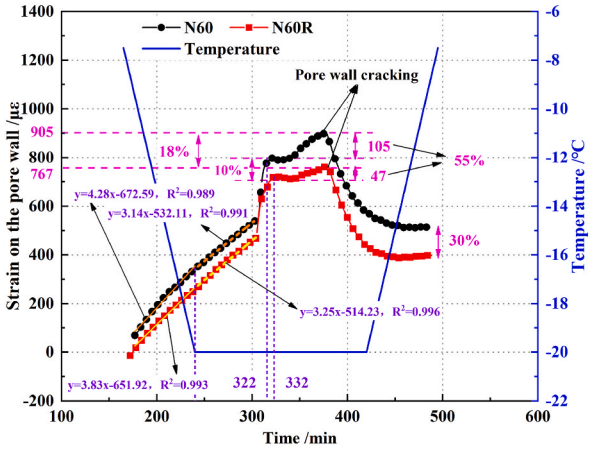

Fig. 15. Strain due to the deterioration of pores of restrained and unrestrained concrete.

(1) The internal damage of restrained concrete induced by SSFT cycles is less severe than that of unrestrained concrete. The increment of IRH and residual strain of the restrained concrete are 30 % lower than those of unrestrained concrete.
(2) One of the reasons for the less severe internal damage of restrained concrete is that the rate of ice crystal formation in restrained concrete is slower than that in unrestrained concrete. This is associated with the weakening of water migration within restrained concrete before the freezing point.
(3) The restraint inhibits the initiation of microcracks from the pore wall by reducing pore deterioration. The important evidence is that the peak strain of pore deterioration in restrained concrete is 18 % lower than that in unrestrained concrete.

CRediT authorship contribution statement

Zhihao Gao: Writing – review & editing, Writing – original draft, Visualization, Methodology, Investigation, Formal analysis, Data curation, Conceptualization. **Zhendi Wang:** Writing – review & editing, Supervision, Resources, Project administration, Funding acquisition. **Ling Wang:** Writing – review & editing, Visualization, Validation, Supervision, Resources, Project administration, Funding acquisition. **Yading Xu:** Writing – review & editing, Methodology. **Xia Zhao:** Project administration, Funding acquisition.

Declaration of competing interest

The authors declare that they have no known competing financial interests or personal relationships that could have appeared to influence the work reported in this paper.

Acknowledgements

The authors acknowledge the financial support of National Key Research and Development Program of China (NO.2022YFB3708700).

Data availability

All data, models, and code generated or used throughout the study appear in the submitted article.

References

[1] A. Shpak, F. Gong, S. Jacobsen, Frost durability of high-volume fly ash concrete: relation liquid transport - damage, Cement Concr. Res. 163 (2023) 107017, https://doi.org/10.1016/j.cemconres.2022.107017.
[2] W. Ruijun, H. Zhiyao, L. Yang, et al., Review on the deterioration and approaches to enhance the durability of concrete in the freeze–thaw environment, Constr. Build. Mater. 321 (2022) 126371, https://doi.org/10.1016/J.CONBUILDMAT.2022.126371.
[3] W. Sun, R. Mu, X. Luo, et al., Effect of chloride salt, freeze–thaw cycling and externally applied load on the performance of the concrete, Cement Concr. Res. 32 (12) (2002) 1859–1864, https://doi.org/10.1016/S0008-8846(02)00769-X.
[4] B.M. Taheri, A.M. Ramezanianpour, S. Sabokpa, et al., Experimental evaluation of freeze-thaw durability of pervious concrete, J. Build. Eng. 33 (2020) 101617, https://doi.org/10.1016/j.jobe.2020.101617.
[5] G. Zhihao, W. Ling, W. Zhendi, et al., Surface features of frost damaged concrete: a study using multi-point micro displacement laser ranging method, J. Build. Eng. 76 (2023) 107051, https://doi.org/10.1016/j.jobe.2023.107051.
[6] S. Fayed, W. M, Structural performance of seas and recycled aggregate concrete filled Solid/Hollow aluminum tubular Columns: an experimental work, Structures 47 (2023) 1323–1340, https://doi.org/10.1016/j.istruc.2022.12.002.
[7] J.J. Valenza, G.W. Scherer, A review of salt scaling: II. Mechanisms, Cement Concr. Res. 37 (7) (2007) 1022–1034, https://doi.org/10.1016/j.cemconres.2007.03.003.

[8] A. Saha, T.M. Tonmoy, MdH.R. Sobuz, et al., Assessment of mechanical, durability and microstructural performance of sulphate-resisting cement concrete over portland cement in the presence of salinity, Constr. Build. Mater. 420 (2024) 135527, https://doi.org/10.1016/j.conbuildmat.2024.135527.
[9] A.M. Maglad, W. Mansour, S. Fayed, et al., Experimental study of the flexural behaviour of RC beams made of eco-friendly sawdust concrete and strengthened by a wooden plate, Int. J. Concr. Struct. Mater. 17 (2023) 49, https://doi.org/10.1186/s40069-023-00617-0.
[10] S. Fayed, E. Madenci, A. Bahrami, et al., Experimental study on using recycled polyethylene terephthalate and steel fibers for improving behavior of RC columns, Case Stud. Constr. Mater. 19 (2023) e02344, https://doi.org/10.1016/j.cscm.2023.e02344.
[11] A.M. Maglad, W. Mansour, B.A. Tayeh, et al., Experimental and analytical investigation of fracture characteristics of steel fiber-reinforced recycled aggregate concrete, Int. J. Concr. Struct. Mater. 17 (2023) 74, https://doi.org/10.1186/s40069-023-00637-w.
[12] ASTM, Standard Test Method for Resistance of Concrete to Rapid Freezing and Thawing, 2015.
[13] ASTM, Standard Test Method for Scaling Resistance of Concrete Surfaces Exposed to Deicing Chemicals, 2003.
[14] S.I. British, Testing Hardened Concrete Part 9: Freeze-Thaw Resistance with De-icing Salts - Scaling, 2016.
[15] M.J. Setzer, P. Heine, S. Kasparek, et al., Test methods of frost resistance of concrete: CIF-Test: capillary suction, internal damage and freeze thaw test—reference method and alternative methods A and B, Mater. Struct. 37 (10) (2004) 743–753, https://doi.org/10.1007/BF02480521.
[16] M.J. Setzer, Frostbelastungsmessung mit Behinderung der Verformungen eines porösen Prüfkörpers, DE Patent, 2014, 14166123.1.
[17] X. Yading, W. Ling, Z. Xia, Analysis of internal frost damage of restrained concrete, in: Proceedings of Recent Advances in Concrete Technology and Sustainability Issues, 2018. Beijing.
[18] G. Zhihao, W. Ling, Z. Xia, Influence of restraint on surface damage of concrete under single-side salt freezing and thawing, J. Chin. Ceram. Soc. 49 (11) (2021) 2494–2501, https://doi.org/10.14062/j.issn.0454-5648.20210142 [In Chinese.].
[19] X. Yading, W. Ling, W. Zhendi, Phenomenon, mechanism and test method of concrete freeze-thaw/salt frost damage, Bull. Chin. Ceram. Soc. 36 (2) (2017) 491–514, https://doi.org/10.16552/j.cnki.issn1001-1625.2017.02.013 [In Chinese.].
[20] X. Yading, Behaviour and Mechanism of Damage Induced by Freeze-Thaw Cycles with Salt Solution of Restrained Concrete, China Building Materials Academy, Beijing, 2017 [in Chinese, dissertation].
[21] M.T. Hasholt, Frost damage of concrete subject to confinement, in: Systems and Structures in Civil Engineering 2016: Segment on Frost Action in Concrete, 2016, pp. 41–49. https://backend.orbit.dtu.dk/ws/portalfiles/portal/126234122/05_MSSCE2016_Word_137.pdf.
[22] T.C. Powers, Air requirement of frost-resistant concrete. Proceedings of the Twenty-Ninth Annual Meeting of the Highway Research Board Held, December 13-16, 1949 at Washington, D.C.
[23] W. Zhendi, Research on the Deterioration Process and Mechanism of Reinforced Concrete on the Basis of Non-destructive Monitoring, China Building Materials Academy, Beijing, 2012 [in Chinese, dissertation].
[24] T.C. Powers, R.A. Helmuth, Theory of volume changes in hardened portland cement paste during freezing, in: Proceedings of the Thirty-Second Annual Meeting of the Highway Research Board, 32, January 13-16, 1953, pp. 285–297. Washington, D.C.
[25] G. Fagerlund, The international cooperative test of the critical degree of saturation method of assessing the freeze/thaw resistance of concrete, Mater. Struct. 10 (4) (1977) 231–253, https://doi.org/10.1007/BF02478694.
[26] G.W. Scherer, Freezing gels, J. Non-Cryst. Solids 155 (1) (1993) 1–25, https://doi.org/10.1016/0022-3093(93)90467-C.
[27] W. Zhendi, Z. Qiang, W. Ling, et al., Characterizing frost damages of concrete with flatbed scanner, Constr. Build. Mater. 102 (2016) 872–883, https://doi.org/10.1016/j.conbuildmat.2015.11.029.
[28] M.J. Setzer, Micro ice lens formation and frost damage, in: Proceedings of the Frost Damage in Concrete, Minneapolis, MN(US), 2002.
[29] H. Luan, J. Wu, J. Pan, Saline water absorption behavior and critical saturation degree of recycled aggregate concrete during freeze-thaw cycles, Constr. Build. Mater. 258 (20) (2020) 119640, https://doi.org/10.1016/j.conbuildmat.2020.119640.
[30] M.J. Setzer, Micro-ice-lens formation in porous solid, J. Colloid Interface Sci. 243 (1) (2001) 193–201, https://doi.org/10.1006/jcis.2001.7828.
[31] V. Penttala, Freezing-induced strains and pressures in wet porous materials and especially in concrete mortars, Adv. Cement Base Mater. 7 (1) (1998) 8–19, https://doi.org/10.1016/S1065-7355(97)00011-4.
[32] Y. Quanbing, Mechanisms of deicer-frost scaling of concrete(I)——capillary-Uptake degree of saturation and ice-formation pressure, J. Build. Mater. 10 (5) (2007) 522–527, https://doi.org/10.3969/j.issn.1007-9629.2007.05.004 [in Chinese].
[33] Y. Quanbing, One of mechanisms on the deicer-frost scaling of concrete (II): degree of saturation and ice-formation pressure during freezing-thawing cycles, J. Build. Mater. 15 (6) (2012) 741–746, https://doi.org/10.3969/j.issn.1007-9629.2012.06.002 [in Chinese].
[34] Z. Liu, W. Hansen, Freeze-thaw durability of high strength concrete under deicer salt exposure, Constr. Build. Mater. 102 (2016), https://doi.org/10.1016/j.conbuildmat.2015.10.194.
[35] Z. Sun, G.W. Scherer, Pore size and shape in mortar by thermoporometry, Cement Concr. Res. 40 (5) (2009) 740–751, https://doi.org/10.1016/j.cemconres.2009.11.011.
[36] Z. Qiang, L. Le, P. Xiaoyun, et al., Freeze–thaw behavior of air entrained cement paste saturated with 10wt.% NaCl solution, Cold Reg. Sci. Technol. 102 (2014) 21–31, https://doi.org/10.1016/j.coldregions.2014.02.003.
[37] Z. Liu, W. Hansen, Freeze-thaw durability of high strength concrete under deicer salt exposure, Constr. Build. Mater. 102 (2016) 478–485, https://doi.org/10.1016/j.conbuildmat.2015.10.194.
[38] D. Xianghui, G. Xiaoyue, W. Ru, et al., Investigation of microstructural damage in air-entrained recycled concrete under a freeze–thaw environment, Constr. Build. Mater. 268 (2021) 121219, https://doi.org/10.1016/j.conbuildmat.2020.121219.
[39] M. Haoxia, Y. Hongfa, D. Bo, et al., Study on failure mechanism of concrete subjected to freeze-thaw condition in airport deicers, Constr. Build. Mater. 313 (2021) 125202, https://doi.org/10.1016/j.conbuildmat.2021.125202.
[40] H. Rui, T. Nantung, N.L. Lu, Unraveling microstructural evolution in air-entrained mortar and paste: insights from MIP and micro-CT tomography amid cyclic freezing-thawing damage, J. Build. Eng. 94 (2024) 109922, https://doi.org/10.1016/j.jobe.2024.109922.
[41] W. Zhendi, Z. Qiang, W. Yuekai, et al., Relative humidity and deterioration of concrete under freeze–thaw load, Constr. Build. Mater. 62 (2014) 18–27, https://doi.org/10.1016/j.conbuildmat.2014.03.027.
[42] S. Zhenhua, G.W. Scherer, Effect of air voids on salt scaling and internal freezing, Cement Concr. Res. 40 (2) (2009) 260–270, https://doi.org/10.1016/j.cemconres.2009.09.027.
[43] G. Zhihao, W. Zhendi, W. Ling, The influence of restraint on salt frost damage of concrete: water migration, J. Chin. Ceram. Soc. 52 (11) (2024) 3361–3371, https://doi.org/10.14062/j.issn.0454-5648.20240358 [in Chinese].
[44] General Administration of Quality Supervision, Inspection and quarantine of the people's Republic of China. Methods for Chemical Analysis of Cement: GB/T 176-2017, Standards Press of China, Beijing, 2017.
[45] General Administration of Quality Supervision, Inspection and Quarantine of the People's Republic of China. Testing Method for Specific Surface of Cement - Blaine Method: GB/T 8074-2008, Standards Press of China, Beijing, 2008.
[46] State Administration for Market Regulation, Test Methods for Water Requirement of Standard Consistency, Setting Time and Soundness of the Portland Cement: GB/T 1346-2024, Standards Press of China, Beijing, 2024.
[47] State Administration for Market Regulation, Test Method of Cement Mortar Strength (ISO Method): GB/T 17671-2021, Standards Press of China, Beijing, 2021.
[48] State Administration for Market Regulation, Sand for Construction: GB/T 14684-2022, Standards Press of China, Beijing, 2022.
[49] Ministry of Housing and Urban Rural Development of the People's Republic of China, Standard for Testing Methods for Physical and Mechanical Properties of Concrete: GB/T 50081-2019, China Construction Industry Press, Beijing, 2019.
[50] Ministry of Housing and Urban Rural Development of the People's Republic of China, Concrete Trial Mold: JG 237-2008, Standards Press of China, Beijing, 2008.
[51] G. Zhihao, Control of Restraint Stress and its Effect on Behavior of Concrete under the Attack of Single-Side Freezing and Thawing, China Building Materials Academy, Beijing, 2020 [in Chinese, dissertation].

[52] Ministry of Housing and Urban Rural Development of the People's Republic of China, Standard for Test Methods for Long Term Performance and Durability of Ordinary Concrete: GB/T 50082-2024, China Construction Industry Press, Beijing, 2024.
[53] H. Yunfen, S. Wubao, W. Ling, et al., Relationship between temperature and relative humidity of concrete during freezing and thawing cycle, J. Build. Eng. 18 (6) (2015) 971–975, https://doi.org/10.3969/j.issn.1007-9629.2015.06.010 [in Chinese].
[54] W. Ling, C. Yin, W. Zhendi, et al., Evolution and characterization of damage of concrete under freeze-thaw cycles, J. Wuhan Univ. Technol.-Materials Sci. Ed. 28 (4) (2013) 710–714, https://doi.org/10.1007/s11595-013-0757-7.
[55] Z. Ge, Study on the Regulation and Mechanisms of Cement Hydration at Negative Temperature, Harbin Institute of Technology, Harbin, 2020 [in Chinese, dissertation].
[56] M. Ru, J. Na, J. Fenfen, Analysis of freeze-thaw cycles test and theoretical study of concrete, Concrete (7) (2016) 145–148, https://doi.org/10.3969/j.issn.1002-3550.2016.07.037 [in Chinese].
[57] H. Nv, Investigation of Concrete Pore Structure and Damage Evolution under Freeze-Thaw Cycles, Chang'an university, Xi'an, 2018 [in Chinese, dissertation].
[58] Z. Zhi Yun, H. Mihashi, Micromechanics model to describe strain behavior of concrete in freezing process, J. Mater. Civ. Eng. 20 (1) (2008) 46–53, https://doi.org/10.1061/(ASCE)0899-1561(2008)20:1(46).
[59] U.A. Campos, D.E. Hall, Simplified Lamé's equations to determine contact pressure and hoop stress in thin-walled press-fits, Thin-Walled Struct. 138 (2019) 199–207, https://doi.org/10.1016/j.tws.2019.02.008.
[60] H. Tou, C. Jie, L. Mi, et al., Investigation on three-dimensional failure criterion of asphalt mixture considering the effect of stiffness, Constr. Build. Mater. 285 (24) (2021) 122431, https://doi.org/10.1016/j.conbuildmat.2021.122431.
[61] Ministry of Housing and Urban Rural Development of the People's Republic of China, Code for Design of Concrete Structures: GB 50010—2015, China Construction Industry Press, Beijing, 2015.